CHEMISTRY
A EUROPEAN JOURNAL

DOI: 10.1002/chem.201100010

Size-Controllable Gold–Platinum Alloy Nanoparticles on Nine Functionalized Ionic-Liquid Surfaces and Their Application as Electrocatalysts for Hydrogen Peroxide Reduction

Yanyan Yu,[a] Qian Sun,[a] Xiaoqian Liu,[a] Haihong Wu,[a] Tianshu Zhou,[b] and Guoyue Shi*[a]

Abstract: A series of room-temperature ionic liquids (RTILs) containing different functional groups such as hydroxyl, nitrile, carboxyl, and thiol attached to imidazolium cations, combined with various anions such as chloride [Cl], tetrafluoroborate [BF_4], hexafluorophosphate [PF_6], and bis-[(trifluoromethyl)sulfonyl]imide [Tf_2N], have been successfully synthesized. Dissolved in chitosan (Chi), the Chi/RTIL composites can be employed as flexible templates for the preparation of Au/Pt nanostructures. These Au/Pt nanostructures can be facilely deposited in situ on the surface of Chi/RTILs through electrodeposition. Scanning electron microscopy (SEM) and atomic force microscopy (AFM) results demonstrate that the alloy size is significantly dependent on the structure of the Chi/RTILs, with sizes ranging from 2.8 to 84.7 nm. Based upon the functionalized RTILs, nine Chi/RTIL–Au/Pt biosensors have been fabricated. First, the size-dependent electrochemistry of Chi/RTIL–Au/Pt was investigated using potassium ferricyanide as the probe. The reversible electron transfer of the $Fe(CN)_6^{3-/4-}$ redox couple was realized for the nine biosensors, and the peak currents, as well as the peak-to-peak separations (ΔE_p) and electron-transfer rates, differ greatly from each other because of the diversity of the RTILs. Further electrochemical research reveals that the functional groups of these RTILs exert an evident influence on the reduction behavior of H_2O_2, which in turn illustrates that the electrocatalytic activity of Chi/RTIL–Au/Pt nanocomposites can be tuned by means of employing RTILs with different functional groups, and an appropriate combination of cations and anions may produce a higher activity. The facilitated electron transfer and the intrinsic catalytic activity of Au/Pt NPs provide a facile way to construct a third-generation H_2O_2 biosensor with a high sensitivity, low detection limit, quick response time, and excellent selectivity.

Keywords: electrocatalysis · electrochemistry · hydrogen peroxide · ionic liquids · nanoparticles · reduction

Introduction

Considerable research interest has been focused on the study of bimetallic nanoalloys because of the additional new properties that may arise from the combination of different compositions of metals on the nanoscale.[1–4] The more favorable properties of bimetallic nanocomposites, which originate from their unique electronic structures, consequently show different catalytic behaviors from their monometallic counterparts, including higher catalytic activity, better resistance to deactivation, and greater catalytic selectivity, for which they have attracted significant attention as electrocatalysts, and as selective oxidation and dehydrogenation catalysts.[5–8] The optical, magnetic, catalytic, and electronic properties of nanoparticles (NPs) are affected not only by their size but also their shape.[9–12] Several methods based on physical (e.g., vapor deposition, laser ablation) and chemical (e.g., metal salt reduction, sol–gel process, micelles) approaches have been developed for the synthesis of nanostructures with controlled size and shape, including nanoalloys.[1,13]

In general, NPs are usually stabilized by electrostatic and/or steric effects. The substrates onto which metal nanostructures are deposited have a significant influence on the morphology and size of the resulting structure, with the substrate in some cases acting as a capping ligand or a stabilizer, and thus playing a key role in NP assemblies.[14] Polymers, micelles, and coordinative ligands have been widely used as stabilizers.[15] These capping ligands or stabilizers can bind strongly to the NP cores, providing great steric hindrance and slowing down the rate of NP growth, and thus

[a] Y. Yu, Q. Sun, X. Liu, H. Wu, Prof. G. Shi
Department of Chemistry and
Shanghai Key Laboratory of Green Chemistry and Chemical Process
East China Normal University
3663 Zhongshan Road (N), Shanghai, 200062 (P. R. China)
Fax: (+86) 021-62237105
E-mail: gyshi@chem.ecnu.edu.cn

[b] T. Zhou
Department of Environmental Science
East China Normal University
3663 Zhongshan Road (N), Shanghai, 200062 (P. R. China)

Supporting information for this article is available on the WWW under http://dx.doi.org/10.1002/chem.201100010.

causing the growth of smaller NPs.[16] The most common binding group is thiol, used with Au or Ag NPs. Other NP binding groups, such as carboxylic acids, amines, phosphines, micelles, and dendrimers, have also been explored for the stabilization of NPs.[17]

Recent results suggest that room-temperature ionic liquids (RTILs) could be preferable solvents in the synthesis and modification of nanostructured materials, because of their unique properties such as the existence of extended hydrogen bonding, good thermal stability, and high ionic conductivity.[18] Transition-metal NPs with small sizes, narrow size distributions, and different shapes have been prepared in RTILs by decomposition of transition-metal complexes in the zero-valent state, metal bombardment, or simple transfer of previously prepared water- or classical organic-solvent-soluble colloids onto the RTILs.[19] A few papers have reported the synthesis and catalytic application of composites of metal NPs and RTILs. Dupont et al. reported an activated iridium NP catalyst in $[C_4mim][PF_6]$ with an average diameter of 2–2.5 nm, which showed clearly improved activity for the biphasic hydrogenation of various olefins and arenes.[20] Other noble metal NP catalysts, such as gold and platinum NPs with tunable sizes synthesized in various imidazolium derivatives, also exhibited remarkably high stabilities in aqueous solutions.[15,21] The non-nucleophilic nature of many RTILs is very advantageous in providing a protective environment for the NPs that can extend the catalyst lifetime.[22] It is believed that RTILs can limit the diffusion of the NPs and thus promote the formation of small particles and limit their growth.[23] Processes involving NP catalysts and RTILs have been particularly effective in screening the charged layer on the surface of the colloids, preventing aggregation and stabilizing the system.[24] By tuning the RTIL compositions, the stability, size, and solubility of the NPs may all be tuned.[25] It is becoming increasingly apparent that the incorporation of functional groups into RTILs is indispensable, as the functional groups can increase catalyst stability and/or improve catalyst retention.[26] Different groups, such as thiols, amines, carboxylic acids, and ethers, could be attached on the cation and/or anion of an RTIL, thereby providing additional stabilization of the NPs due to their coordination on the metal surface.[27] Ionic liquids with cationic or anionic special functional groups act not only as reducing agents, but also as reaction media for the synthesis of AuNPs and polymer–AuNP composites.[28] Moreover, a number of critical aspects of RTILs make them an interesting medium in which enzymes and even living cells can retain their bioactivities, which therefore provides a facile route for the preparation of new biosensors.[29]

In this work, we introduce hydroxyl, nitrile, carboxyl, and thiol functionalities into the imidazolium cation, and combine the resulting cations with various anions, including chloride [Cl], tetrafluoroborate $[BF_4]$, hexafluorophosphate $[PF_6]$, and bis[(trifluoromethyl)sulfonyl]imide $[Tf_2N]$ (Scheme 1). For ease of comparison, we divide the nine RTILs into two groups according to the combinations of cation and anion. $[C_3(OH)_2mim][BF_4]$, $[C_3(OH)_2mim][PF_6]$, $[C_3(OH)_2mim][Tf_2N]$, and $[C_3(OH)_2mim][Cl]$ are in Group I, having the same cation but different anions. $[C_3(OH)_2mim][Cl]$, $[C_3CNmim][Cl]$, $[C_3COOHmim][Cl]$, $[C_3OHmim][Cl]$, and $[C_3(OCOCH_2SH)_2mim][Cl]$ belong to Group II, possessing the same anion, but with different functional groups attached to the imidazolium core. Furthermore, $[C_3CNmim][BF_4]$ was also synthesized, as it was required as a comparison of the optimal anion in Group I and cation in Group II for the reduction of H_2O_2. The physical properties of the corresponding RTILs (thermogravimetry, conductivity, etc.) were explored. In this paper, we use these functionalized RTILs as both stabilizers and templates for the size-controlled preparation of Au/Pt alloy NPs. By dissolving these RTILs in chitosan (Chi), nine Chi/RTIL film-based Chi/RTIL–Au/Pt biosensors were fabricated directly on glassy carbon (GC) electrodes through the electrodeposition method. Electrochemical experiments demonstrated that reversible electron transfer of the $Fe(CN)_6^{3-/4-}$ redox couple was realized for all of the nine biosensors, and the peak currents, as well as peak-to-peak separations (ΔE_p) and electron-transfer rates, differed greatly from each other for different Chi/RTIL structures. In addition, the electrocatalytic activity of Chi/RTIL–Au/Pt films toward H_2O_2 also showed a Chi/RTIL-dependent process, as confirmed by linear sweep voltammetry (LSV). Consequently, these RTIL–Au/Pt nanocomposites were successfully constructed for use in a third-generation H_2O_2 biosensor.

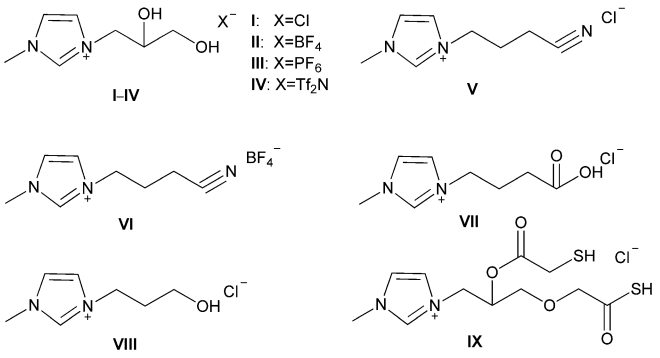

Scheme 1. Structures of the nine RTILs utilized in the present study. The $[N(CF_3SO_2)_2]^-$ anion is abbreviated as Tf_2N^-. **I**: 1-(2′,3′-dihydroxypropyl)-3-methylimidazolium chloride, $[C_3(OH)_2mim][Cl]$. **II**: 1-(2′,3′-dihydroxypropyl)-3-methylimidazolium tetrafluoroborate, $[C_3(OH)_2mim]$ $[BF_4]$. **III**: 1-(2′,3′-dihydroxypropyl)-3-methylimidazolium hexafluorophosphate, $[C_3(OH)_2mim][PF_6]$. **IV**: 1-(2′,3′-dihydroxypropyl)-3-methylimidazolium bis[(trifluoromethyl)sulfonyl]imide, $[C_3(OH)_2mim][Tf_2N]$. **V**: 1-(3′-cyanopropyl)-3-methylimidazolium chloride, $[C_3CNmim][Cl]$. **VI**: 1-(3′-cyanopropyl)-3-methylimidazolium tetrafluoroborate, $[C_3CNmim][BF_4]$. **VII**: 1-(3′-carboxylpropyl)-3-methylimidazolium chloride, $[C_3COOHmim][Cl]$. **VIII**: 1-(3′-hydroxypropyl)-3-methylimidazolium chloride, $[C_3OHmim]$ $[Cl]$. **IX**: 1-(2′,3′-dimercaptoacetoxypropyl)-3-methylimidazolium chloride, $[C_3OCO(CH_2)SHmim][Cl]$.

Results and Discussion

Physical characterization of electrical conductivity, electrochemical window, and thermal stability of the prepared RTILs: The majority of RTILs have a σ value of 10^{-3} S cm^{-1} at room temperature (25 ± 1 °C), which is much lower than conventional aqueous electrolytes applied in electrochemistry. In general, ionic liquids based on imidazolium cations usually have a higher conductivity in comparison with those based on tetraalkylammonium, pyrrolidinium, piperidinium, and pyridinium cations.[30] Factors influencing the conductivity include the viscosity, density, temperature, and so on.[29] The conductivities and viscosities of the nine RTILs were all measured at room temperature, and the data are collected in Table 1. Generally, the room-temperature conductivities are situated in the range 0.11–0.68 S m^{-1}, with the maximum value of 0.68 for $[C_3(OH)_2mim][BF_4]$, and the minimum of 0.11 for $[C_3(OCOCH_2SH)_2mim][Cl]$. In Group I, for the same cation, the conductivities according to the anions have the following order: $[BF_4]^- > [Cl]^- > [PF_6]^- > [Tf_2N]^-$. This order is inversely related to the viscosities. The specific conductivity order for the five cations in Group II is: $[C_3CNmim]^+ > [C_3COOHmim]^+ > [C_3(OH)_2mim]^+ > [C_3OHmim]^+ > [C_3(OCOCH_2SH)_2]^+$. It is worth noting that some RTILs do not obey the inverse relationship between viscosity and conductivity well. For example, $[C_3(OH)_2mim][Cl]$ possesses a σ value of 0.49 S m^{-1}, and is accompanied by a comparatively high viscosity. One possible reason may be the presence of ion pairs or ion aggregates in some RTILs, which would reduce the Coulombic attractive force between ions and decrease the viscosity accordingly.[31] Actually, Galinski et al. stated in their review that the inverse relationship between conductivity and viscosity may be more applicable to electrolytes than RTILs, because the model of an ionic liquid is based on the assumption that the RTIL consists entirely of ions, and neglects the possibility of ion pairs or ion aggregates.[31] However, it should be pointed out that ion pairs and neutral ion aggregates cannot contribute to the ionic conductivity, as clarified in previous reports.[32,33] Thus, the detected conductivities in our experiments should all be ascribed to the isolated cations and anions. This point is of vital importance for an explanatory parameter. From the σ results, we find that although $[C_3CNmim][Cl]$ and $[C_3COOHmim][Cl]$ have higher conductivities than the other three RTILs, the ionic conductivities are still lower than that of $[C_3(OH)_2mim][BF_4]$. An evident decrease in conductivity could be seen for $[C_3(OCOCH_2SH)_2mim][Cl]$ (0.11 S m^{-1}). This can be explained by its higher viscosity, which probably hinders the ion mobility. It is notable that although the RTILs containing $[C_3CNmim]^+$ and $[BF_4]^-$ show the highest ionic conductivities in Groups I and II, respectively, their assembly as $[C_3CNmim][BF_4]$ show a σ value of 0.45 S m^{-1}, lower than those of both $[C_3(OH)_2mim][BF_4]$ and $[C_3CNmim][Cl]$. These results also suggest that the conductivity depends upon the combination of cations and anions rather than the individual ions. Generally speaking, the excellent conductivities may make RTILs promising solvents that can be exploited to realize galvanization or electrolysis that cannot be carried out in conventional solvents.

The oxidation and reduction potentials and the electrochemical window were also determined in this work. It is known that electrolytes for application in electrochemical devices should be resistant to the electrochemical reduction and oxidation that is the essence of most electrochemical reactions. The electrochemical stability for most RTILs determined at glassy carbon or platinum electrode is within the range 4.0–6.0 V.[34] The RTILs investigated herein display an electrochemical window from 4.3 to 5.4 V, as shown in Table 1. The results show that in Group I, $[C_3(OH)_2mim][Cl]$ possesses a remarkably wider electrochemical window than the other three RTILs. It is worth noting that the increase in the electrochemical stability for $[C_3(OH)_2mim][Cl]$ benefits from the co-enhancement of the anodic potential of Cl^- and the cationic potential of $[C_3(OH)_2mim]^+$, whereas the amide anion, $[N(CF_3SO_2)_2]^-$ (abbreviated to Tf_2N), is oxidized at relatively low anodic potentials compared with BF_4^- and PF_6^-. Almost all RTILs in Group II undergo anodic oxidation at relatively high potentials, except for $[C_3OHmim][Cl]$, the oxidation process of which occurs at just 2.3 V. The results also illustrate that either the oxidation or reduction potential is determined by the counterion effect, rather than the single cations or anions in the RTILs.

The thermal stability of the RTILs after the incorporation of functional groups was also investigated. The upper temperature limit for most RTILs depends mainly upon the decomposition temperature (T_d: the temperature at which the weight loss of the RTIL in an aluminum pan under a N_2 atmosphere reaches 5%). The T_d values of the nine RTILs employed in this work range from 260 to 345 °C. The TG

Table 1. Physical properties of the nine functionalized RTILs.

	Conductivity [S m^{-1}]	Viscosity [Pa s]	T_d [°C]	Anodic voltage [V]	Cathodic voltage [V]	Electrochemical window [V]	Trace amounts of Cl^- [mol kg^{-1}]
$[C_3(OH)_2mim][BF_4]$	0.68	5.05	260	2.3	−2.2	4.5	0.010
$[C_3(OH)_2mim][PF_6]$	0.44	8.05	275	2.5	−2.2	4.7	0.015
$[C_3(OH)_2mim][Tf_2N]$	0.20	11.43	290	2.2	−2.2	4.4	0.010
$[C_3(OH)_2mim][Cl]$	0.49	6.13	345	2.9	−2.5	5.4	–
$[C_3CNmim][Cl]$	0.59	0.37	307	2.7	−2.6	5.3	–
$[C_3COOH][Cl]$	0.56	0.02	310	2.8	−1.9	4.7	–
$[C_3OHmim][Cl]$	0.38	0.54	315	2.3	−2.0	4.3	–
$[C_3(OCOCH_2SH)_2mim][Cl]$	0.11	3.30	305	2.5	−2.0	4.5	–
$[C_3CNmim][BF_4]$	0.45	0.39	300	2.5	−2.5	5.0	0.015

curves show that all nine RTILs display a one-step weight-loss process with a noticeable change detected, indicating high thermal stability over a wide range of temperatures (figures not shown). General tendencies can be summarized from the results in Table 1. For Group I, the relative thermal stabilities according to anions are in the order $[Cl]^- > [Tf_2N]^- > [PF_6]^- > [BF_4]^-$. For Group II, the relative thermal stabilities according to cations are $[C_3(OH)_2mim]^+ > [C_3OHmim]^+ > [C_3COOHmim]^+ > [C_3CNmim]^+ > [C_3(OCOCH_2SH)_2mim]^+ > [C_3CNmim][BF_4]$. Among these nine RTILs, $[C_3(OH)_2mim][Cl]$ shows the highest thermal stability ($T_d = 345\,°C$), and $[C_3(OH)_2mim][BF_4]$ has the lowest thermal stability ($T_d = 260\,°C$).

Characterization of Au/Pt nanostructures electrodeposited on nine Chi/RTILs: Figure 1 shows SEM micrographs of the assembled Au/Pt nanostructures deposited on the nine Chi/RTIL films. It is evident that, except for the $[C_3(OH)_2mim][Tf_2N]$-based Au/Pt nanocomposite (Figure 1 Ic), all the other Au/Pt nanocomposites exist in the form of NPs, with their sizes varying following the variation in the RTILs. The respective diameters, ranging from 2.8 to 84.7 nm, are listed in Table 3 (see later). Among these, a diameter of 2.8 nm is estimated for the $[C_3(OH)_2mim][BF_4]$-based Au/Pt NPs, and the largest particle of 84.7 nm is produced on the $[C_3OHmim][Cl]$ film. In Group I, for $[C_3(OH)_2mim][BF_4]$ [I(a)], the Au/Pt NPs are uniformly distributed on the $[C_3(OH)_2mim][BF_4]$ film with no agglomeration, and are well isolated from each other. Larger particle sizes and more densely assembled Au/Pt NPs are obtained on the $[C_3(OH)_2mim][Cl]$ film (Figure 1 Id). A large portion of the scattered NPs start to coalesce in the case of $[C_3(OH)_2mim][PF_6]$, leading to an evident increase in the particle size. For $[C_3(OH)_2mim][Tf_2N]$, however, the NPs seem to form a kind of compact cluster with a highly irregular geometry, so it becomes difficult for us to measure a single particle. For Group II, as demonstrated in Figure 1 IIa–e, well-dispersed NPs are formed on the $[C_3(OH)_2mim][Cl]$ (Figure 1Id), $[C_3CNmim][Cl]$ (Figure 1 IIa), $[C_3CNmim][BF_4]$ (Figure 1 IIb), and $[C_3(OCOCH_2SH)_2mim][Cl]$ (Figure 1 IIe) films. On the other hand, for both the $[C_3COOHmim][Cl]$ (Figure 1 IIc) and $[C_3OHmim][Cl]$ (Figure 1 IId) films, different increases in the Au/Pt particle size are observed, between which the $[C_3OHmim][Cl]$-based nanostructure display relatively more evident coagulations, the average size of which reaches nearly 84.7 nm. These results unambiguously indicate that the functional groups linked to the imidazolium core were highly accessible with distinct stabilization abilities for bimetallic nanostructures.

Four representative two-dimensional AFM images, obtained in tapping mode, are shown in Figure 2 for $[C_3(OH)_2mim][Cl]$- (A), $[C_3CNmim][BF_4]$- (B), $[C_3CNmim][Cl]$- (C), and $[C_3(OCOCH_2SH)_2mim][Cl]$-stabilized (D) Au/Pt NPs. These images display the explicit topography and distribution of Au/Pt nanostructures deposited on the Chi/RTIL films. The reason for selecting these four typical Chi/RTILs as the model is related mainly to their similar diameters, as found from SEM results. For the $[C_3(OH)_2mim][Cl]$-based Chi/RTIL–Au/Pt system (Figure 2 A), the NPs are uniformly distributed on the Chi/RTIL film with no agglomeration, and are generally isolated with little interconnection. The average vertical height is around 15 nm. On the other hand, for the other three Chi/RTIL–Au/Pt nanocomposites, different degrees of agglomeration of the NPs are

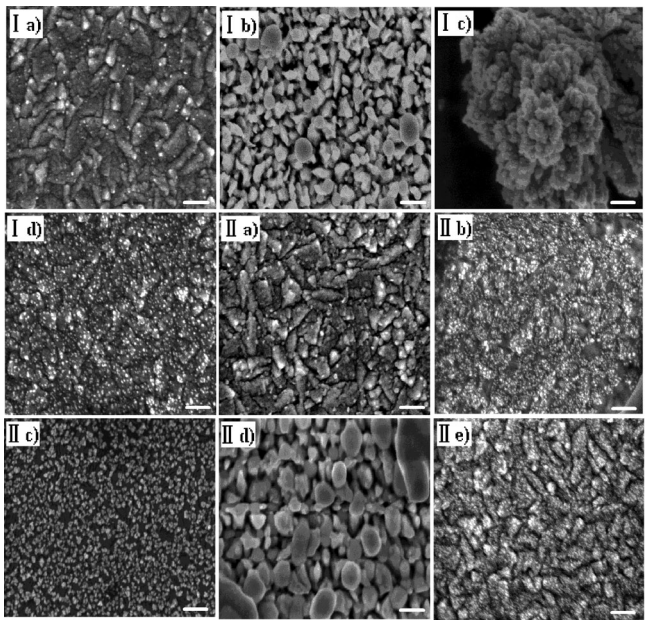

Figure 1. SEM images of nine Chi/RTIL–Au/Pt nanocomposites obtained on ITO. I and II represent Groups I and II. Ia) $[C_3(OH)_2mim][BF_4]$; Ib) $[C_3(OH)_2mim][PF_6]$; Ic) $[C_3(OH)_2mim][Tf_2N]$; Id) $[C_3(OH)_2mim][Cl]$; IIa) $[C_3CNmim][Cl]$; IIb) $[C_3CNmim][BF_4]$; IIc) $[C_3COOHmim][Cl]$; IId) $[C_3OHmim][Cl]$; IIe) $[C_3(OCOCH_2SH)_2mim][Cl]$. All the scale bars represent 100 nm.

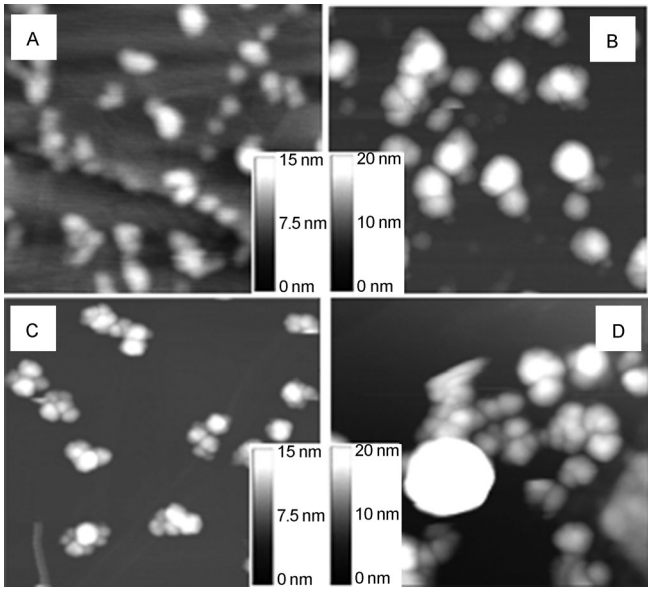

Figure 2. Typical AFM images of four Chi/RTIL–Au/Pt nanocomposites obtained on HOPG. A) $[C_3(OH)_2mim][Cl]$; B) $[C_3CNmim][BF_4]$; C) $[C_3CNmim][Cl]$; D) $[C_3(OCOCH_2SH)_2mim][Cl]$.

observed, among which the $[C_3CNmim][Cl]$ film (Figure 2C) and $[C_3(OCOCH_2SH)_2mim][Cl]$ (Figure 2D) are more severe than $[C_3CNmim][BF_4]$ (Figure 2B), on which the Au/Pt NPs interconnect compactly with each other. However, generally speaking, the particle height measured by AFM is basically consistent with the particle diameter estimated by SEM. The above results indicate that the structural tuning of Chi/RTILs may also provide a powerful strategy for preparing various morphologies of metal nanostructures.

It is known that capping agents or cross-linkers play a significant role in stabilizing NPs, either by binding strongly to the NPs through electrostatic attraction or providing great steric bulk, which can slow down the growth rate of NPs and thus lead to the formation of smaller particles.[16] For some kinds of stabilizers, the lone pair of electrons at the nitrogen and oxygen atoms in the groups of the structure can be donated into two sp hybrid orbitals of the metal ions, thus forming complex ions.[35] The competition between the two mechanisms determines the ultimate size and morphology of the particles. In our experiment, Au/Pt NPs were firstly attracted from bulk solution onto the Chi/RTIL film, which were initially sufficiently small and well separated from each other with little interconnection. Then, the nanoparticles began to grow in size and increase in number. Whether the particles were stabilized through electrostatic attraction or coordination with functional groups still needs to be discussed. For Group I, we take $[C_3(OH)_2mim][BF_4]$ as an example. A conductivity of 0.68 $S\,m^{-1}$ was achieved, and its stabilized Au/Pt NPs, with a particle size of 2.8 nm, were well dispersed on the film. We assume that the upstanding conductivity provides a favorable conducting membrane matrix for stabilizing Au/Pt particles. The increase in the number of mobile positively and negatively charged ions is beneficial for strengthening the interaction with $AuCl_4^-$ and $PtCl_6^-$ through electrostatic forces. The conductivity sequence in Group I was $[BF_4]^- > [Cl]^- > [PF_6]^- > [Tf_2N]^-$, which coincided well with the diameter sequence from the SEM results. The situation became slightly more complex for Group II. The listed conductivity sequence deviated totally from the obtained SEM results, indicating the failure of the electrostatic attraction application in this case. We are apt to think that the stabilization is probably achieved through the coordination effect between the two sp hybrid orbitals of the metal ions and the functional groups of the RTILs. The ability to coordinate with Au/Pt tailors the final size of the Au/Pt NPs. For example, the lone-pair electrons existing on the two hydroxyl groups or the nitrile group in the structures of $[C_3(OH)_2mim][Cl]$ and $[C_3CNmim][BF_4]$ or $[C_3CNmim][Cl]$ facilitate the donation of electrons to the hybrid orbitals of the metal ions, which reinforces the coordination and leads to the formation of well-dispersed smaller NPs. On the other hand, the relatively poor coordination ability of carboxyl compared with hydroxyl and nitrile groups results in the occurrence of NP aggregates. The known binding capability of SH-terminated functional groups toward Au NPs is also well exhibited in this work. Further investigations of the interaction between metal ions and functional groups in Chi/RTILs are still in progress in our laboratory.

Electrochemical techniques were also adopted for further characterization of the Chi/RTIL-stabilized Au/Pt NPs. The cyclic voltammetry behaviors of electron-transfer indicators, such as $Fe(CN)_6^{3-/4-}$, were first studied for the nine Chi/RTIL–Au/Pt modified electrodes and compared with that at a Au/Pt-modified electrode, as shown in Figure 3A. The peak-to-peak separations (ΔE_p) are listed in Table 2. The

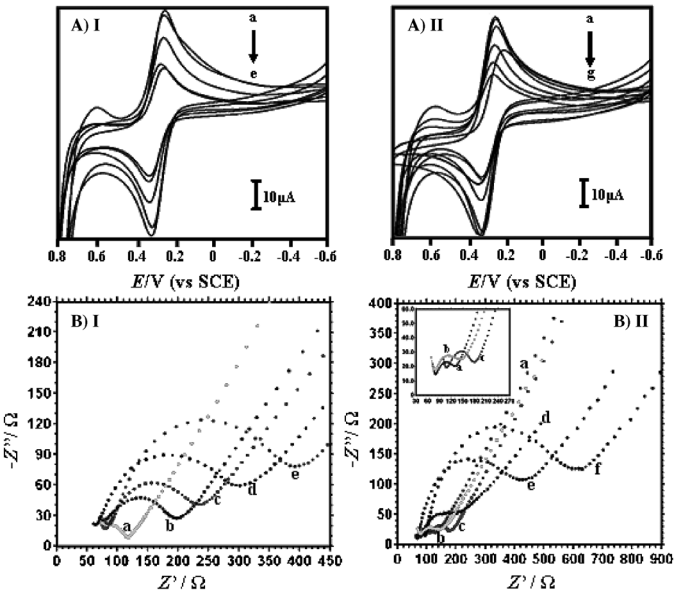

Figure 3. A) Cyclic voltammograms obtained at Chi/RTIL–Au/Pt-GC in 0.1 M KCl solution containing 1 mM $K_3Fe(CN)_6$. I and II represent Groups I and II. a, b, c, d, and e in I correspond to $[C_3(OH)_2mim][BF_4]$, $[C_3(OH)_2mim][Cl]$, bare GC, $[C_3(OH)_2mim][PF_6]$, and $[C_3(OH)_2mim][Tf_2N]$, respectively; a, b, c, d, e, f, and g in II represent $[C_3CNmim][BF_4]$, $[C_3CNmim][Cl]$, $[C_3COOHmim][Cl]$, $[C_3(OH)_2mim][Cl]$, bare GC, $[C_3(OCOCH_2SH)_2mim][Cl]$, and $[C_3OHmim][Cl]$, respectively. B) Nyquist plots obtained at Chi/RTIL–Au/Pt-GC in 0.1 M KCl solution containing 1 mM $[Fe(CN)_6]^{3-/4-}$. RTILs a, b, c, d, and e in I correspond to $[C_3(OH)_2mim][BF_4]$, $[C_3(OH)_2mim][Cl]$, without Chi/RTIL, $[C_3(OH)_2mim][PF_6]$, and $[C_3(OH)_2mim][Tf_2N]$, respectively. RTILs a, b, c, d, e, and f in II represent $[C_3CNmim][BF_4]$, $[C_3(OH)_2mim][Cl]$, $[C_3CNmim][Cl]$, $[C_3COOHmim][Cl]$, $[C_3(OCOCH_2SH)_2mim][Cl]$, and $[C_3OHmim][Cl]$, respectively. Inset graph shows the amplified images for a, b, and c.

Table 2. Results of electrochemical experiments performed in 0.1 M KCl solution containing 1 mM $K_3Fe(CN)_6$ for Au/Pt- and Chi/RTIL–Au/Pt-modified electrodes.

	I_p [μA]	ΔE_p [mV]	Electroactive surface area [10^{-6} cm^2]
Au/Pt (without RTIL)	−27.04	73	122.80
$[C_3(OH)_2mim][BF_4]$	−37.51	66	170.35
$[C_3(OH)_2mim][PF_6]$	−18.64	61	84.65
$[C_3(OH)_2mim][Tf_2N]$	−18.02	75	81.83
$[C_3(OH)_2mim][Cl]$	−35.86	69	162.85
$[C_3CNmim][Cl]$	−36.41	91	165.35
$[C_3COOH][Cl]$	−21.86	62	99.27
$[C_3OHmim][Cl]$	−16.49	63	74.89
$[C_3(OCOCH_2SH)_2mim][Cl]$	−17.11	60	77.70
$[C_3CNmim][BF_4]$	−41.51	75	188.51

quasi-reversible redox behavior of ferricyanide, and near unity of the anodic-to-cathodic peak current ratio (I_p^a/I_p^c), which is typical of the reversible process of the redox species in solution phase, are observed at Chi/RTIL–Au/Pt- and Au/Pt-modified electrodes. ΔE_p for the Au/Pt-modified electrode is 73 mV. For Group I (Figure 3A I), four Chi/RTIL-based electrodes display different redox behaviors primarily in terms of their peak currents and ΔE_p values. Among them, $[BF_4]^-$ (curve a) and $[Cl]^-$ (curve b) show enhanced peak currents compared with the Au/Pt electrode, with their ΔE_p values of 69 and 66 mV, respectively. However, less favorable results are obtained for $[PF_6]^-$ (curve c) and $[Tf_2N]^-$ (curve d), which exhibit much lower peak currents relative to Au/Pt-GC. The results are in good agreement with the conductivity sequence. Similar phenomena also occur for the Chi/RTILs in Group II (Figure 3A II). The peak currents are in the order $[C_3CNmim][BF_4] > [C_3CNmim][Cl] > [C_3COOHmim]^+ > [C_3(OH)_2mim]^+ > [C_3(OCOCH_2SH)_2mim]^+ > [C_3OHmim]^+$, partially coinciding with the conductivity sequence, except for $[C_3CNmim][BF_4]$, the conductivity of which is ranked further back while it achieves the highest current value in Group II. Moreover, apart from $[C_3(OCOCH_2SH)_2mim][Cl]$ (curve f) and $[C_3OHmim][Cl]$ (curve g), the peak currents for the other four Chi/RTILs are higher than the bare Au/Pt-GC. This may be explained by the preferable conductivities and smaller diameters of Au/Pt NPs stabilized with them. The poor conductivities of $[C_3(OCOCH_2SH)_2mim][Cl]$ and $[C_3OHmim][Cl]$ make them disadvantageous in terms of improving the redox current and promoting electron transfer between Fe^{2+} and Fe^{3+}. The above results show that the redox process for a given substance at Chi/RTIL–Au/Pt surfaces is tunable as a function of the kind of RTIL.

The influence of the kind of Chi/RTIL on the electron-transfer rate of $[Fe(CN)_6]^{3-/4-}$ was also investigated through electrochemical impedance spectroscopy (EIS), as shown in Figure 3B. The charge-transfer resistance (R_{ct}) of the $[Fe(CN)_6]^{3-/4-}$ redox couple is around 230 Ω at the bare Au/Pt-GC (curve c). This value decreases to 120 and 190 Ω for the $[BF_4]^-$- (curve a) and $[Cl]^-$-based (curve b) films, respectively, and increases to 300 and 400 Ω for $[PF_6]^-$ (curve c) and $[Tf_2N]^-$ (curve d), respectively. In addition, for Chi/RTILs in Group II (Figure 3B II), electron transfer is greatly facilitated at $[C_3CNmim][BF_4]$-, $[C_3(OH)_2mim]^+$-, $[C_3CNmim][Cl]$-, and $[C_3COOHmim]^+$-based nanostructure surfaces, corresponding to R_{ct} values of 130, 150, 170, and 200 Ω, respectively. However, a tremendous increase in R_{ct} is observed for $[C_3(OCOCH_2SH)_2mim]^+$ and $[C_3OHmim]^+$, with values of 450 and 600 Ω, respectively. The distinct differences in R_{ct} at the nine Chi/RTIL-modified nanostructure surfaces, intrinsically reflecting the ability of the Chi/RTILs to enhance the electron-transfer rate, are in good agreement with the results obtained in Figure 3A. The results also serve as a verification of the accuracy of the detection method employed in this experiment.

Comparison of electrochemical responses toward hydrogen peroxide with different Chi/RTIL-modified electrodes: Most metal NP electrocatalysts have been evaluated for both the methanol oxidation and oxygen reduction reactions.[36–38] In the light of the fact that the functional groups of the Chi/RTILs have a significant influence on the Au/Pt NP particle sizes, it is therefore in our interest to investigate what role these different functionalized Chi/RTILs may play on the electrocatalytic behavior of some kind of substance. Here, we take H_2O_2 as the probe. Figure 4 presents a typical set of LSV curves recorded between −0.5 and +0.6 V at the nine Chi/RTIL–Au/Pt-GC electrodes in 0.1 M PBS (pH 7.4), with (curve a) and without (curve b) 0.5 mM H_2O_2. Evident differences could be seen for the nine electrodes with respect to the peak shape, the reductive peak potential (E_{pa}), and the magnitude of the reduction current. The specific reductive peak potentials and the values of the reduction currents are given in Table 3. On the whole, well-defined reduction waves between 0 and −0.2 V could be seen at $[C_3(OH)_2mim][BF_4]$- (Figure 4A), $[C_3(OH)_2mim][PF_6]$- (Figure 4B), $[C_3(OH)_2mim][Cl]$- (Figure 4D), $[C_3COOHmim][Cl]$- (Figure 4E), and $[C_3CNmim][Cl]$-based (Figure 4F) electrodes. Of these, $[C_3(OH)_2mim][BF_4]$ and $[C_3COOHmim][Cl]$ show a much more positive reductive potential in comparison with the other two. Comparatively speaking, the reductive potential for $[C_3CNmim][Cl]$ is relatively broad, suggesting a sluggish redox process for H_2O_2. For the other four Chi/RTILs, that is, $[C_3(OH)_2mim][Tf_2N]$ (Figure 4C), $[C_3OHmim][Cl]$ (Figure 4G), $[C_3(OCOCH_2SH)_2mim][Cl]$ (Figure 4H), and $[C_3CNmim][BF_4]$ (Figure 4I), however, the characteristic reduction peaks are either shaped irregularly or disappeared completely. In light of the response toward the same concentration of H_2O_2, the current responses are arranged in the following orders: for Group I, the sequence is $[BF_4]^- > [Cl]^- > [PF_6]^- > [Tf_2N]^-$; for Group II, the result is $[C_3(OH)_2mim]^+ > [C_3COOH]^+ > [C_3CNmim][Cl] > [C_3OHmim]^+ > [C_3CNmim][BF_4] > [C_3(OCOCH_2SH)_2mim]^+$. It is notable that, among these nine Chi/RTIL-based electrodes, the $[C_3(OH)_2mim][BF_4]$-based electrode shows the most active electrocatalytic behavior toward the reduction of H_2O_2, as verified from the favorable conductivity of 0.68 $S\,m^{-1}$ and the particle diameter of 2.8 nm for $[C_3(OH)_2mim][BF_4]$. It is generally accepted that the reduction efficiency is controlled by both the electroactive surface area of the electrode and the conductivity of the base material. The specific electroactive surface area for Chi/RTIL–Au/Pt-GC can be calculated according to the Randles–Sevcik equation [Eq. (1)], in which D is the diffusion coefficient ($cm^2\,s^{-1}$), n is the electron stoichiometry, C is the bulk concentration of the electroactive substance, A is the electroactive surface area (cm^2), and v is the potential scan rate ($V\,s^{-1}$).

$$I_p = 2.69 \times 10^5 A D^{1/2} n^{3/2} v^{1/2} C \quad (1)$$

Assuming $D = 1.0 \times 10^{-5}\ cm^2\,s^{-1}$, $n = 1$, $v = 0.1\ V\,s^{-1}$, and $C = 1$ mM, the electroactive surface areas for all the Chi/

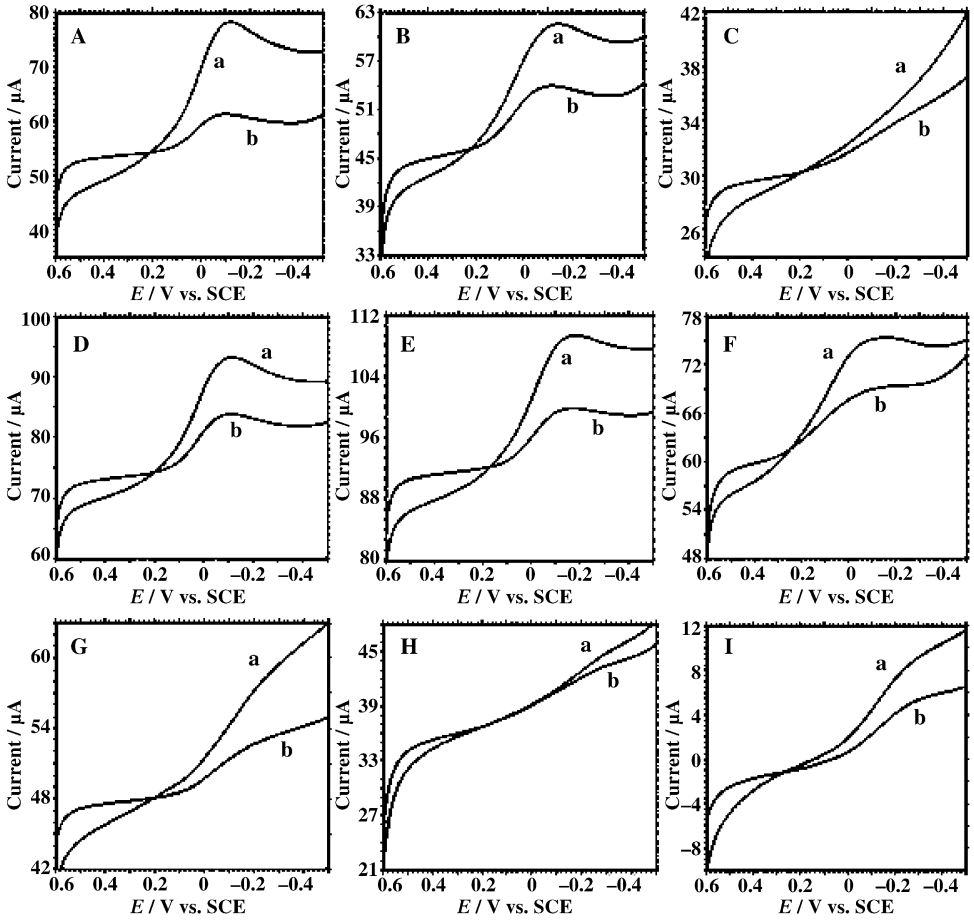

Figure 4. Comparison of LSV responses of the nine Chi/RTIL–Au/Pt-modified electrodes toward 0.5 mM H_2O_2 in a) 0.5 mM H_2O_2 in PBS, and b) blank 0.1 M PBS (pH 7.4). RTILs: A) $[C_3(OH)_2mim][BF_4]$, B) $[C_3(OH)_2mim][PF_6]$, C) $[C_3(OH)_2mim][Tf_2N]$, D) $[C_3(OH)_2mim][Cl]$, E) $[C_3COOHmim][Cl]$, F) $[C_3CNmim][Cl]$, G) $[C_3OHmim][Cl]$, H) $[C_3(OCOCH_2SH)_2mim][Cl]$, and I) $[C_3CNmim][BF_4]$.

Table 3. Influence of the nine functionalized RTILs on the diameter (mean ± S.D.), the surface area of Au/Pt NPs estimated from SEM and AFM analysis, and the different electrochemical responses toward 0.5 mM H_2O_2 obtained from LSV experiments. Reduction currents were obtained by subtracting the current magnitude measured in 0.5 mM H_2O_2 solution from that in blank PBS solution.

	Diameter of Au/Pt [nm]	Surface area of Au/Pt [m^2g^{-1}]	Reductive peak potential [mV]	Reduction current [μA]
$[C_3(OH)_2mim][BF_4]$	2.8 ± 0.3	100.13	−93	9.78
$[C_3(OH)_2mim][PF_6]$	36.8 ± 10.5	7.62	−115	6.83
$[C_3(OH)_2mim][Tf_2N]$	–	–	–	0.78
$[C_3(OH)_2mim][Cl]$	13.7 ± 2.1	20.47	−100	8.97
$[C_3CNmim][Cl]$	18.4 ± 4.2	15.24	−166	6.21
$[C_3COOHmim][Cl]$	23.4 ± 5.5	11.98	−70	7.30
$[C_3OHmim][Cl]$	84.7 ± 14.2	3.31	–	2.63
$[C_3(OCOCH_2SH)_2mim][Cl]$	19.7 ± 7.3	14.23	–	0.98
$[C_3CNmim][BF_4]$	14.6 ± 4.8	19.21	–	2.60

RTIL–Au/Pt based electrodes were calculated, and are summarized in Table 2. It is evident from the results that the modification of Au/Pt NPs onto the Chi/RTIL films plays a key role in enhancing the electroactive surface area. In addition, compared with pure Au/Pt NPs, the electrodes modified with composite Chi/RTIL–Au/Pt exhibit a discrepant ability to enhance the electroactive surface area, which is induced by the variation in the RTILs. For example, in Group I, only $[BF_4]^-$- and $[Cl]^-$-based electrodes show a higher surface area compared with that obtained on Au/Pt GC. For Group II, $[C_3COOH]^+$-, $[C_3OHmim]^+$-, and $[C_3(OCOCH_2SH)_2mim]^+$-based electrodes display remarkably lower surface areas. Taking $[C_3(OCOCH_2SH)_2mim]^+$ as an example, it is found that, besides the poor conductivity (0.11 $S\,m^{-1}$), the huge bulk of the $OCOCH_2SH$ group probably produces a blocking effect on the electron transfer between the electrode and the substrate, which is another major disadvantageous factor influencing the electrocatalytic behavior. It is notable that although BF_4^-- and $[C_3(OH)_2mim]^+$-based electrodes show the best electrocatalytic activities for the reduction of H_2O_2 in their respective groups, the combination of these ions does not provide as good electrocatalysis as expected. Thus, we can draw a further conclusion that the electrocatalytic activity can be tuned by simply, but effectively, selecting an appropriate combination of cation and anion within the structure of RTILs when employing Chi/RTIL and metal NP systems. The cations or anions individually cannot determine these properties.

Amperometric measurements for H_2O_2 with the $[C_3(OH)_2mim][BF_4]$–Au/Pt-modified electrode: In view of the good catalytic properties of the $[C_3(OH)_2mim][BF_4]$–Au/Pt nanomaterials characterized above, the amperometric detection of H_2O_2 with $[C_3(OH)_2mim][BF_4]$ was implemented, as shown in Figure 5.

Firstly, to investigate whether the co-fabrication of $[C_3(OH)_2mim][BF_4]$ and Au/Pt nanocomposites onto a bare GC electrode could enhance the amperometric response toward H_2O_2, we recorded the current responses with $[C_3(OH)_2mim][BF_4]$-Au- (Figure 5A curve a), $[C_3(OH)_2mim][BF_4]$–Au/Pt- (curve b), $[C_3(OH)_2mim][BF_4]$-

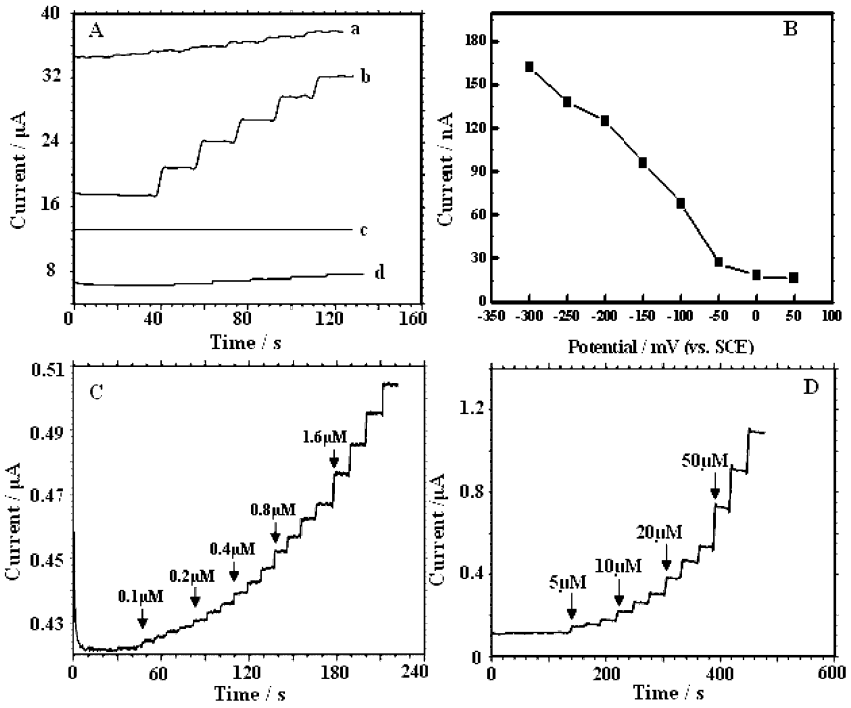

Figure 5. A) Current–time responses toward 50 μM H_2O_2 in 0.1 M PBS (pH 7.4) at a) $[C_3(OH)_2mim][BF_4]$-Au-, b) $[C_3(OH)_2mim][BF_4]$–Au/Pt-, c) $[C_3(OH)_2mim][BF_4]$-, and d) $[C_3(OH)_2mim][BF_4]$-Pt-modified electrodes at a working potential of −200 mV. B) Dependence of the responses of the $[C_3(OH)_2mim][BF_4]$–Au/Pt electrode to 50 μM H_2O_2 on different working potentials from −300 to +50 mV. Current–time plots of $[C_3(OH)_2mim][BF_4]$–Au/Pt-modified electrode on successive addition of specific concentrations of H_2O_2 from C) 0.1 to 12 μM, and D) 5 to 250 μM at a working potential of −200 mV.

(curve c), and $[C_3(OH)_2mim][BF_4]$-Pt-modified (curve d) electrodes at −200 mV toward 50 μM H_2O_2 in a well-stirred PBS solution (0.1 M, pH 7.4). No visible reduction current is found with the $[C_3(OH)_2mim][BF_4]$-modified electrode, and only about 50 and 70 nA of current responses at $[C_3(OH)_2mim][BF_4]$-Pt- and $[C_3(OH)_2mim][BF_4]$-Au-modified electrodes, respectively, are observed with each addition of 50 μM H_2O_2. The reduction current is increased almost sixfold to about 300 nA at the $[C_3(OH)_2mim][BF_4]$–Au/Pt-modified electrode compared to the other three electrodes. This result is associated with the excellent electrocatalytic activity of the Au/Pt alloy toward H_2O_2 reduction. Meanwhile, the electrocatalytic activity of Au/Pt alloy NPs has been proved to be better than their monometallic counterparts, which could be ascribed to the synergistic effect of Au and Pt in the alloy NPs.

Figure 5B shows the dependency of the amperometric responses of $[C_3(OH)_2mim][BF_4]$–Au/Pt-modified electrode toward 50 μM H_2O_2 on different working potentials. The measurements were made in a stirred buffer solution, and the currents were recorded point by point at each potential from +50 to −300 mV. As shown, the amperometric current responses increase slowly with the increase of operating potential from +50 to −50 mV. Then it starts to rise rapidly from −100 to −300 mV. Considering the fact that, with the negative shift of the potential, the noise of the background also increases and the interferences from oxygen and ascorbic acid reductions may occur, we selecte −200 mV as the optimal working potential in the following experiments.

The current versus time plots in Figure 5C and D display the responses of the $[C_3(OH)_2mim][BF_4]$–Au/Pt electrode to the successive addition of H_2O_2 into 0.1 M PBS (pH 7.4) at −200 mV. It is seen that, with H_2O_2 addition into the stirred buffer solution, the sensor responds rapidly and then reaches a steady state, achieving 95% of the steady-state current within 10 s. The current response to H_2O_2 is found to exhibit two linear ranges. The first range is between 0.1 and 12 μM (I [nA] = 1.66 C [μM] + 3.36, R^2 = 0.994), with a sensitivity of (3.36 ± 1.02) nA μM^{-1}. The second range is linear from 5 μM to 0.25 mM (I [nA] = 0.91 C [μM] + 20.09, R^2 = 0.999), with a sensitivity of (20.09 ± 1.93) nA μM^{-1}. Moreover, the detection limit, estimated to be 60 nM (S/N = 3), is much lower than those published previously.[39,40] This wide linear range and low detection limit can be ascribed to the good conductivity of $[C_3(OH)_2mim][BF_4]$ and the high electrocatalytic activity of the Au/Pt nanocomposite.

Additionally, the selectivity for the determination of H_2O_2 with the $[C_3(OH)_2mim][BF_4]$–Au/Pt-modified electrode was also evaluated (Figure S1, Supporting Information). Ascorbic acid (AA) and dopamine (DA) are considered to be the major interferences both to an online sensor and to an in vivo probe, because of their high concentrations and low oxidation potentials. The results show that the physiological concentrations of 0.2 mM of AA and 10 μM of DA do not produce measurable current responses at the operating potential of −200 mV in the presence of H_2O_2, which indicates that the measurement of H_2O_2 is essentially free from the interference of these electroactive species, thus providing a reliable way to detect real biological samples in the future.

The reproducibility of the response of the $[C_3(OH)_2mim][BF_4]$–Au/Pt electrode to 50 μM H_2O_2 was also examined (Figure S2, Supporting Information). The RSD value for the amperometric currents (n = 30) is 2.21%, indicating excellent repeatability under the mentioned conditions. Moreover, the biosensor retains almost 86% of its initial activity after being stored at +4 °C for two weeks, demonstrating its excellent long-term stability.

Conclusion

Chi/RTIL-stabilized Au/Pt alloy NPs with controllable sizes in the range of 2.8 to 84.7 nm were prepared in situ by tuning the functional groups in the RTIL structures. Subsequently, not only the particle size, but also the electrochemical process of potassium ferricyanide on Chi/RTIL–Au/Pt nanocomposite films, was shown to depend strongly on the structure of the RTIL with respect to reversibility, peak current, and electron-transfer rate. In addition, the electrocatalytic activity of Chi/RTIL–Au/Pt films toward H_2O_2 could also be tuned by employing different RTILs as the base material. The electrochemical properties of Chi/RTILs are dependent on the combination of cations and anions, not on either of them individually. The present study provides a methodology for achieving the highest catalytic activity for a certain substance using functionalized RTILs and metal NPs. More importantly, the facilitated electron transfer and the intrinsic catalytic activity of Au/Pt NPs showed that the functionalized RTILs can act as highly effective media for the preparation and stabilization of metal nanoparticles, thus providing another facile route for the development of a non-enzyme H_2O_2 biosensor with high sensitivity and long stability.

Experimental Section

Reagents: *N*-Methylimidazole, 3-chloro-1,2-propanediol, NH_4PF_6, lithium bis[(trifluoromethyl)sulfonyl]imide, 3-chloro-1-propanol, and methyl 4-chlorobutyrate were all obtained from Shanghai Darui Finechemical Co. (China). Hydrogen tetrachloroaurate hydrate ($HAuCl_4 \cdot 3H_2O$, 99.9%, 1 g/5 mL) and hexachloroplatinate ($H_2PtCl_6 \cdot 6H_2O$, 99.9%, 1 g/5 mL) were obtained from Shanghai Chemical Reagent Company (Shanghai, China). 30% H_2O_2 was obtained from Beijing Chemical Co. (China). All other reagents were of at least analytical grade and used without further purification. The chitosan solution (0.5%) was prepared by dissolving chitosan (0.050 g) in acetic acid solution (2.0 M, 10 mL). The supporting electrolyte was 0.1 M phosphate buffer solution (PBS) prepared with 0.1 M Na_2HPO_4 and 0.1 M KH_2PO_4, and the pH value was adjusted to 7.4 with NaOH. All other solutions were prepared with doubly distilled water.

Instruments and measurements: The morphologies of the nine functionalized RTIL-based Chi/RTIL–Au/Pt nanocomposites were studied on a BioScope atomic force microscope (AFM) (NanoScope IIIa SPM System, Digital Instruments, Inc., USA) and scanning electron microscope (SEM) (Hitachi Co. Ltd., Tokyo, Japan). AFM measurements were carried out in air in tapping mode using standard silicon AFM probes (Mikromasch Ultrasharp NSC11/AIBS) having cantilever spring constants of 1.5–5.0 $N\,m^{-1}$ and resonance frequencies from 45 to 75 kHz. Elemental analyses (carbon, hydrogen, and nitrogen) were performed using a CE Instruments EA-1110 elemental analyzer. The thermal decomposition temperatures (T_d) for a 5% weight loss were assessed by employing a TGA 851e/SF/1100 analyzer at a heating rate of $10\,°C\,min^{-1}$ under a flowing N_2 atmosphere. NMR spectra were measured on a Bruker DMX 400 instrument, using $SiMe_4$ for ^1H and ^{13}C NMR as an external standard at 25 °C. Viscosities were measured with an Ubbelohde viscometer. The temperature of the samples was maintained at (25 ± 1) °C by means of an external temperature controller. The measurements were performed three times and an average value was obtained. Conductivity measurements were performed in a two-platinum-electrode conductivity cell (cell constant $K_{cell} = 0.68$, determined by aqueous KCl standard solution), under thermostated bath conditions. The measurement was repeated three times and the average value was calculated. The amounts of traces of Cl^- in $[C_3(OH)_2mim][BF_4]$, $[C_3(OH)_2mim][PF_6]$, $[C_3(OH)_2mim][Tf_2N]$, and $[C_3CNmim][BF_4]$ were measured using the Vollhard method. Electrochemical experiments were performed on a CHI 832 electrochemical workstation (CHI Company, USA), with a conventional three-electrode system composed of a platinum wire as the counter electrode, a saturated calomel electrode (SCE) (Jiangsu Electroanalytical Instruments Factory, China) as the reference electrode, and a bare or modified glassy carbon electrode as the working electrode.

Preparations of Chi/RTIL-stabilized Au/Pt nanostructures and Chi/RTIL–Au/Pt electrodes: Nine Chi/RTIL-stabilized Au/Pt nanostructures were prepared through electrochemical deposition. Before modification, a glassy carbon electrode (2 × 1.5 cm) was polished with alumina paste (0.05 μm) on a microcloth, subsequently cleaned ultrasonically with acetone, NaOH (1:1), HNO_3 (1:1), and doubly distilled water, and then dried at room temperature ((25 ± 1) °C). For the preparation of Chi/RTIL-stabilized Au/Pt nanostructures, the nine functionalized RTILs (10 μL) were first respectively dispersed in chitosan (1 mL, 0.5%) solution with the aid of ultrasonic agitation to form well-distributed mixed solutions. Then, 5 μL of the mixture was dropped onto the cleaned glassy carbon electrode, and was allowed to dry at ambient temperature. Electrochemical deposition of Au/Pt NPs was performed in H_2SO_4 (0.5 M) aqueous solution containing $HAuCl_4$ (81 μM) and H_2PtCl_6 (0.16 mM). The potential was set at −1.0 V and the deposition time was 50 s. To decrease the size and prevent the aggregation of the Au/Pt NPs, the electrodeposition procedure was performed in an ice-bath environment, and ultrasonic irradiation was applied to give a more uniform composition. The resulting RTIL–Au/Pt electrodes were carefully rinsed with doubly distilled water and allowed to dry at room temperature. When the modified electrodes were not in use, they were stored at 4 °C.

Acknowledgements

We sincerely thank the program from the Science & Technology Commission of Shanghai Municipality (10JC1404000), State 863 projects (2009AA064201), and the Fundamental Research Funds for the Central Universities. This work was also supported by Funding from the Shanghai Key Laboratory of Green Chemistry and Chemical Processes of ECNU.

[1] V. Abdelsayed, A. Aljarash, M. S. El-Shall, *Chem. Mater.* **2009**, *21*, 2825–2834.
[2] E. I. Santiago, L. C. Varanda, H. M. Villullas, *J. Phys. Chem. C* **2007**, *111*, 3146–3151.
[3] H. Q. Li, G. Q. Sun, N. Li, S. G. Sun, D. S. Su, Q. Xin, *J. Phys. Chem. C* **2007**, *111*, 5605–5617.
[4] S. Koh, P. Strasser, *J. Am. Chem. Soc.* **2007**, *129*, 12624–12625.
[5] J. Zhang, K. Sasaki, E. Sutter, R. R. Adzic, *Science* **2007**, *315*, 220–222.
[6] A. Habrioux, E. Sibert, K. Servat, W. Vogel, K. B. Kokoh, N. A. Vante, *J. Phys. Chem. B* **2007**, *111*, 10329–10333.
[7] J. B. Xu, T. S. Zhao, Z. X. Liang, L. D. Zhu, *Chem. Mater.* **2008**, *20*, 1688–1690.
[8] D. S. Shephard, T. Maschmeyer, G. Sankar, J. M. Thomas, D. Ozkaya, B. F. G. Johnson, R. Raja, R. D. Oldroyd, R. G. Bell, *Chem. Eur. J.* **1998**, *4*, 1214–1225.
[9] J. A. Creighton, D. G. Eadon, *J. Chem. Soc. Faraday Trans.* **1991**, *87*, 3881–3891.
[10] S. Link, M. A. El-Sayed, *J. Phys. Chem. B* **1999**, *103*, 8410–8426.
[11] Z. L. Wang, *J. Phys. Chem. B* **2000**, *104*, 1153–1175.
[12] Y. W. Cao, R. Jin, C. A. Mirkin, *J. Am. Chem. Soc.* **2001**, *123*, 7961–7968.
[13] S. Park, J. Joo, S. G. Kwon, Y. Jang, T. Hyeon, *Angew. Chem.* **2007**, *119*, 4714–4745; *Angew. Chem. Int. Ed.* **2007**, *46*, 4630–4660.
[14] T. M. Day, P. R. Unwin, J. V. Macpherson, *Nano Lett.* **2007**, *7*, 51–57.
[15] K. S. Kim, D. Demberelnyamba, H. Lee, *Langmuir* **2004**, *20*, 556–560.

[16] A. Zabet-Khosousi, A. A. Dhirani, *Chem. Rev.* **2008**, *108*, 4072–4124.
[17] H. P. Liang, T. G. J. Jones, N. S. Lawrence, L. Jiang, J. S. Barnard, *J. Phys. Chem. C* **2008**, *112*, 4327–4332.
[18] K. Biswas, C. N. R. Rao, *Chem. Eur. J.* **2007**, *13*, 6123–6129.
[19] H. Wender, L. F. de Oliveira, P. Migowski, A. F. Feil, E. Lissner, M. H. G. Prechtl, S. R. Teixeira, J. Dupont, *J. Phys. Chem. C* **2010**, *114*, 11764–11768.
[20] J. Dupont, G. S. Fonseca, A. P. Umpierre, P. F. P. Fichtner, S. R. Teixeira, *J. Am. Chem. Soc.* **2002**, *124*, 4228–4229.
[21] H. Itoh, K. Naka, Y. Chujo, *J. Am. Chem. Soc.* **2004**, *126*, 3026–3027.
[22] V. I. Pârvulescu, C. Hardacre, *Chem. Rev.* **2007**, *107*, 2615–2665.
[23] a) D. J. Brauer, K. Kottsieper, C. Liek, O. Stelzer, H. Waffenschmidt, P. Wasserscheid, *J. Organomet. Chem.* **2001**, *630*, 177–184; b) K. Kottsieper, O. Stelzer, P. Wasserscheid, *J. Mol. Catal. A.* **2001**, *175*, 285–288; c) J. Sirieix, M. Ossberger, B. Betzemeier, P. Knochel, *Synlett* **2000**, 1613–1615.
[24] P. J. Dyson, *Coord. Chem. Rev.* **2004**, *248*, 2443–2458.
[25] D. Astruc, F. Lu, J. R. Aranzaes, *Angew. Chem.* **2005**, *117*, 8062–8083; *Angew. Chem. Int. Ed.* **2005**, *44*, 7852–7872.
[26] Z. F. Fei, D. B. Zhao, D. Pieraccini, W. H. Ang, T. J. Geldbach, R. Scopelliti, C. Chiappe, P. J. Dyson, *Organometallics* **2007**, *26*, 1588–1598.
[27] J. Dupont, J. D. Scholten, *Chem. Soc. Rev.* **2010**, *39*, 1780–1804.
[28] W. Huang, S. M. Chen, Y. S. Liu, H. Y. Fu, G. Z. Wu, *Nanotechnology* **2011**, *22*, 025602.
[29] M. Galínski, A. Lewandowski, I. Stepniak, *Electrochim. Acta* **2006**, *51*, 5567–5580.
[30] Q. H. Zhang, Z. P. Li, J. Zhang, S. G. Zhang, L. Y. Zhu, J. Yang, X. P. Zhang, Y. Q. Deng, *J. Phys. Chem. B* **2007**, *111*, 2864–2872.
[31] A. Noda, K. Hayamizu, M. Watanabe, *J. Phys. Chem. B* **2001**, *105*, 4603–4610.
[32] W. Wang, R. Balasubramanian, R. W. Murray, *J. Phys. Chem. C* **2008**, *112*, 18207–18216.
[33] D. P. Kaur, K. Yamada, J. S. Park, S. S. Sekhon, *J. Phys. Chem. B* **2009**, *113*, 5381–5390.
[34] A. Lewandowski, A. Świderska-Mocek, *J. Power Sources* **2009**, *194*, 601–609.
[35] I. Pastoriza-Santos, L. M. Liz-Marzan, *Adv. Funct. Mater.* **2009**, *19*, 679–688.
[36] J. Luo, P. N. Njoki, Y. Lin, D. Mott, L. Y. Wang, C. J. Zhong, *Langmuir* **2006**, *22*, 2892–2898.
[37] Y. S. Hu, Y. G. Guo, W. Sigle, S. Hore, P. Balaya, J. Maier, *Nat. Mater.* **2006**, *5*, 713–717.
[38] X. H. Kang, Z. B. Mai, X. Y. Zou, P. X. Cai, J. Y. Mo, *Anal. Biochem.* **2007**, *369*, 71–79.
[39] C. M. Welch, C. E. Banks, A. O. Simm, R. G. Compton, *Anal. Bioanal. Chem.* **2005**, *382*, 12–21.
[40] J. S. Huang, D. W. Wang, H. Q. Hou, T. Y. You, *Adv. Funct. Mater.* **2008**, *18*, 441–448.

Received: January 3, 2011
Published online: August 18, 2011

